

Highlights

Controlling Tip Vortices and Cavitation through Tip Permeability for Tidal Turbines

Yabin Liu,Junchen Tan,Richard H. J. Willden,Paul Gary Tucker,Ignazio Maria Viola

- A novel approach of controlling tip vortices through permeable tip treatment is proposed and investigated.
- There is an optimal range of permeability that can suppress the pressure-drop with the tip vortices by up to 63%.
- Permeable tip treatment shows great potential for breaking the upper tip-speed ratio limit capped by cavitation.
- The vortex intensity is mitigated because of the enhanced vortex diffusion and enlarged vortex dimension.

Controlling Tip Vortices and Cavitation through Tip Permeability for Tidal Turbines

Yabin Liu^{a,b,*}, Junchen Tan^{a,b}, Richard H. J. Willden^c, Paul Gary Tucker^a and Ignazio Maria Viola^b

^aDepartment of Engineering, University of Cambridge, Cambridge, CB2 1PZ, UK

^bSchool of Engineering, University of Edinburgh, Edinburgh, EH9 3BF, UK

^cDepartment of Engineering Science, University of Oxford, Oxford, OX1 3PJ, UK

ARTICLE INFO

Keywords:

Tidal Turbines
Wind Turbines
Tip Vortices
Cavitation
Permeability

ABSTRACT

Blade-tip vortices can lead to wakes, cavitation and noise, and their control remains a significant challenge for tidal and wind turbines. In the present work, we propose controlling tip vortices through local permeability on a model-scale horizontal-axis turbine. The numerical investigation follows a rigorous validation and verification process. The tip permeability is modelled by including a porous zone over the blade tip, within which Darcy's law is applied. The results demonstrate that there is an optimal range of permeability, corresponding to a non-dimensional Darcy number, Da , of around 10^{-5} , that can substantially decrease the tip vortex intensity. The revealed flow physics show that the permeable tip can effectively enlarge the vortex viscous core radius with little change to the vortex circulation. The permeable tip treatment can increase the minimal pressure-coefficient at the vortex core by up to 63%, which significantly alleviates the cavitation risk. This approach has negligible influence on the turbine's energy-harvesting performance because the spanwise extent of the permeable zone is only in the order of 0.1% turbine diameter. Our findings demonstrate this approach's great promise to break the upper tip-speed ratio limit capped by cavitation for tidal turbines, contributing to developing more efficient and resilient turbines.

1. Introduction

Harnessing the power of renewable sources, such as wind and oceans, stands as a crucial stride in our world's transition to net zero. Global Wind Energy Council (2024) states that wind energy now meets around 10% of global electricity demand, a milestone driven by substantial contributions from countries like China, which alone added 75 GW, accounting for two-thirds of the new capacity worldwide in 2023. In addition, tidal power shows great potential to serve as a significant part of the renewable energy scheme in future, meeting 11% of annual electricity demands in the UK (Coles, Angeloudis, Greaves et al. (2021)). However, wind and tidal turbines, which are critical for converting renewable energy into electricity, face significant challenges related to blade-tip vortices. Tip vortices arise from the pressure difference across the wing or blade tip, creating a trailing swirl, shown in Figure 1. These vortices, along with the associated wake (Lignarolo, Ragni, Scarano, Ferreira and Van Bussel (2015); Posa, Broglia and Balaras (2021)), cavitation (Liu, Tan and Wang (2018); Wimshurst, Vogel and Willden (2018); Wang, Bai, Qian, Cheng and Ji (2022)), and noise (Ramachandran, Raman and Dougherty (2014); Bai, Cheng and Ji (2022)) problems, can greatly impact the efficiency and resilience of wing- and blade-based systems, such as underwater vehicles and turbine rotors. In particular, tidal turbines operate underwater and their blade tips experience the highest flow speed, and thus cavitation occurs due to low pressure inside the tip vortices at a high tip speed ratio (TSR). Moreover, the risk of blade erosion and damage is high due to the corrosive nature of seawater (Hou, Ren, Zhang, Dong, An, Zhao, Zhou and Chen (2020)). These problems constrain the further increase of the turbines' TSR, which is beneficial for both aero-hydrodynamic efficiency and reducing the size of powertrain components (Ning and Dykes (2014); Wimshurst et al. (2018)).

In turbomachinery, two primary types of tip flows can occur: tip leakage vortices, when there is a gap between a rotating blade tip and casing wall, and tip vortices when there is no casing wall. Despite their differences, the underlying

*Corresponding author

✉ y1742@cam.ac.uk (Y. Liu)

🌐 <https://www.eng.cam.ac.uk/profiles/y1742> (Y. Liu)

ORCID(s): 0000-0002-0150-5671 (Y. Liu)

Controlling Vortices through Tip Permeability

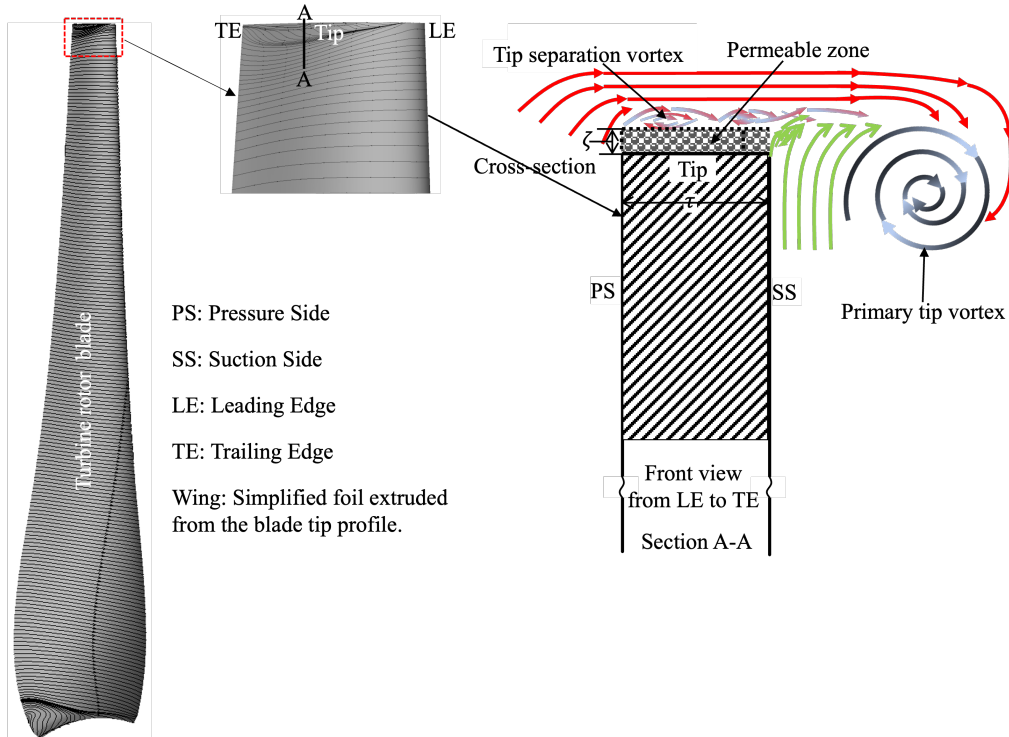


Figure 1: Schematic of tip vortices and permeable tip treatment on a tidal turbine blade. ζ denotes the spanwise scope of the permeable zone; τ denotes the blade tip thickness.

physics of these vortices share remarkable similarities. The intensity of tip (leakage) vortices, which is closely related to the local pressure-drop around the vortex core (Ye, Wang and Shao (2023); Dreyer, Decaix, Münch-Alligné and Farhat (2014)) and the vortex breakdown (Posa, Viola and Broglia (2024); Liu, Wang, Tan, Tucker and Möller (2024)), has a dominant influence on the cavitation risks, flow unsteadiness, and wake recovery. To suppress the primary tip leakage vortex (PTLV), we introduced local micro-jets passively generated by a groove at the tip to interfere with the PTLV, and this approach shows a significant potential to suppress the PTLV and associated cavitation (Liu and Tan (2020, 2018); Han, Liu and Tan (2022)). However, the experimental work followed by Jiang, Xie, Xu, Li and Huang (2022) shows that the shrinking groove added on the tip may generate new cavitation because of the high local flow speed inside the groove itself. This suggests that the groove design needs to be improved by avoiding centralising the jet flow inside a single groove.

Bio-inspired research in natural systems, such as the flight of dandelion seeds, has demonstrated the critical role of permeability and porosity in controlling vortical structures (Cummins, Seale, Macente, Certini, Mastropaolo, Viola and Nakayama (2018); Bose, Bruce and Viola (2023)). Inspired by the above, we propose a novel approach to controlling tip vortices with permeable tip treatment, aiming to mitigate the intensity of tip vortices and the associated cavitation risks. The tip permeability, modelled by a confined porous zone as shown in Figure 1, allows low-speed flows going through the permeable zone driven by the pressure difference between the pressure side (PS) and the suction side (SS), and these flows will further interfere with the primary tip vortex (PTV). This is similar to the shrinking groove design (Liu and Tan (2018)), but without the risks of new cavitation inside the groove. It also allows the numerical examination of the control effect across a wide range of permeability.

Existing studies by Khorrani, Li and Choudhari (2002) and Palleja-Cabre, Saraceno, Paruchuri and Joseph (2022) for controlling tip leakage vortices using porous media focus specifically on the influence of porosity on the tip leakage noises in turbomachinery. A recent experimental and numerical work by Bi, Bao, Zhang, Shao and Li (2024) on tip leakage cavitation around a foil demonstrates the promising potential of using the porous tip to mitigate cavitation, but they focused on tip leakage vortices across a range of tip gap sizes, and the role of permeability was not discussed. Furthermore, recent studies on porous coating around cylinders by Arcondoulis, Liu, Ragni, Avallone, Rubio-Carpio,

Sedaghatizadeh, Yang and Li and finlet rails on wing trailing-edge by Fisciatti, Pereira and Ragni demonstrated that permeable structures have the potential to significantly mitigate vortex-induced noise.

In the present work, we propose controlling tip vortices, particularly the pressure-drop at the vortex core, through a confined permeable treatment. This approach is not limited to new blade designs utilising porous materials but can also be applied to structural modifications, such as incorporating multiple holes or grooves, to introduce a certain degree of tip permeability. By allowing controlled permeability at the blade tips, these designs aim to mitigate the intensity of tip vortices and reduce the associated risks of cavitation, wake, and noise. We apply a steady blade-resolved Reynolds-averaged Navier-Stokes (RANS) approach to model a horizontal-axis tidal turbine and compare it to the existing data from experimental measurements (Willden, Chen, Harvey, Edwards, Vogel, Bhavsar, Allsop, Gilbert, Mullings, Ghobrial et al. (2023)), as described in Section 3 and Appendix A. The tip permeability is modelled by changing the momentum equation in terms of adding the flow resistance in porous cell zone, and a wide range of permeability is applied and discussed. In Section 4.1 and Section 4.2, the vortex structures, minimal pressure-coefficient at the vortex core are compared and discussed to conclude the optimal permeability for mitigating cavitation risks. In Section 4.3, the influence of permeable tip treatment on the turbine power and thrust coefficients is also discussed. Finally, an investigation into the vortex parameters is performed to reveal the underlying physics.

2. Case Configuration and Methodology

2.1. Turbine rotor simulation

In the present work, we model a third of a tidal turbine rotor (Figure 2) under a non-inertial rotating frame of reference using Computational Fluid Dynamics (CFD) simulations. The model-scale turbine, tested by the UK Supergen Offshore Renewable Energy Hub (Willden et al. (2023)), has a rotor diameter of 1.6 m. The experiments were performed in a towing tank at a Reynolds number of 1.3×10^6 based on the constant towing velocity $U_\infty = 1 \text{ m s}^{-1}$ and the turbine diameter. The turbine blade span is 0.7 m, and the blade tip-chord length is 0.043 m.

We solve the steady-state Reynolds-averaged Navier-Stokes (RANS) equations and employ the SST $k - \omega$ turbulence model within *Ansys Fluent 2023R1*. The computational domain is a 120° slice of a cylinder, whose axis coincides with that of the tested turbine. The domain has a radius of $2.5D$. A rotor-stator interface is placed between the rotor domain and the stationary computational domain. The distance between the inlet and the front of the rotor hub, as well as the distance between the rear of the rotor hub and the outlet, is set to $6D$ in the streamwise direction. Uniform, constant free stream velocity with low turbulence is set at the upstream inlet boundary; constant zero pressure is set at the downstream outlet boundary; periodic condition applied at the two inner side boundaries to account for the adjacent passages; slip condition applied at the outer side boundary; and no-slip condition at the blade and hub. The SIMPLEC scheme is used to decouple pressure and velocity in solving the governing equations of incompressible flow. Second-order discretisation schemes are applied for gradients. A second-order scheme is used for pressure, and second-order upwind schemes are applied to the momentum equations, turbulence kinetic energy, and specific dissipation rate.

ICEM-CFD is employed to discretise the computational domain with a structural mesh of around 17 million hexahedral cells (Figure Figure 3). The blade boundary layer is resolved with the averaged y^+ below 1 at the design tip-speed ratio $\lambda = 6.03$, and the y^+ distribution on the blade surface is demonstrated in Figure 3c. The growth ratio of the grid size inside the blade boundary layer is around 1.1 along the wall-normal direction. A total of 150 nodes are distributed along the blade tip in the chordwise direction, 45 nodes in the thickness direction, and 20 nodes in the spanwise direction within the permeable zone.

2.2. Permeable zone simulation

The permeable tip treatment is modelled by including a porous zone over the blade tip section. This porous zone is defined as a separate fluid zone in the computational domain and designated as a porous medium. As shown in Figure 3d, the interface between the permeable tip and the surrounding flow field is treated using conformal mesh to ensure continuity in velocity and pressure fields.

To model the permeability in this zone, we used the built-in porous media model in *Fluent*, where the momentum sink term is defined based on the Darcy model. In this model, the pressure loss due to the porous medium is proportional to the local velocity, representing viscous resistance only. The sink term added to the momentum equation takes the form:

$$\mathbf{S} = -\frac{\mu}{\kappa} \mathbf{u}$$

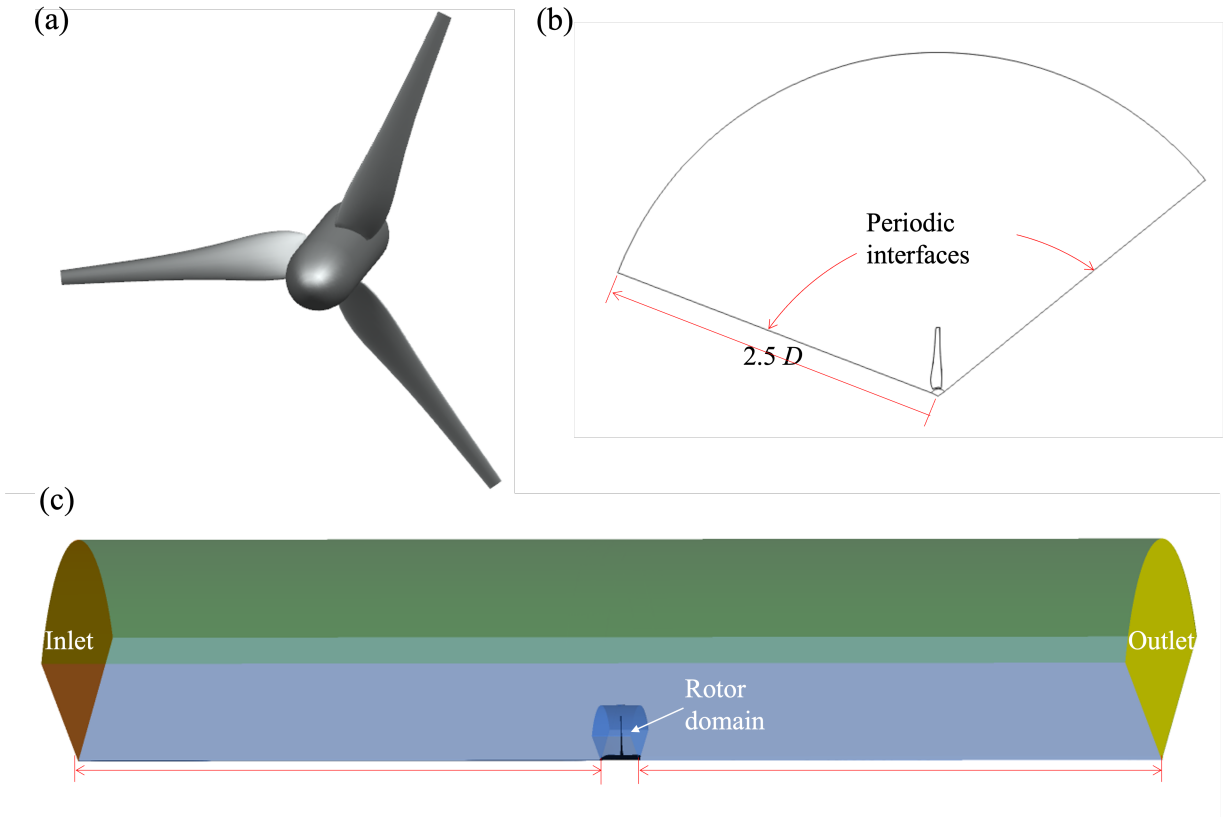


Figure 2: Modelled turbine rotor: (a) the complete geometry; (b) axial view of the 120°-wedge computational domain. (c) three-dimensional view of the computational domain.

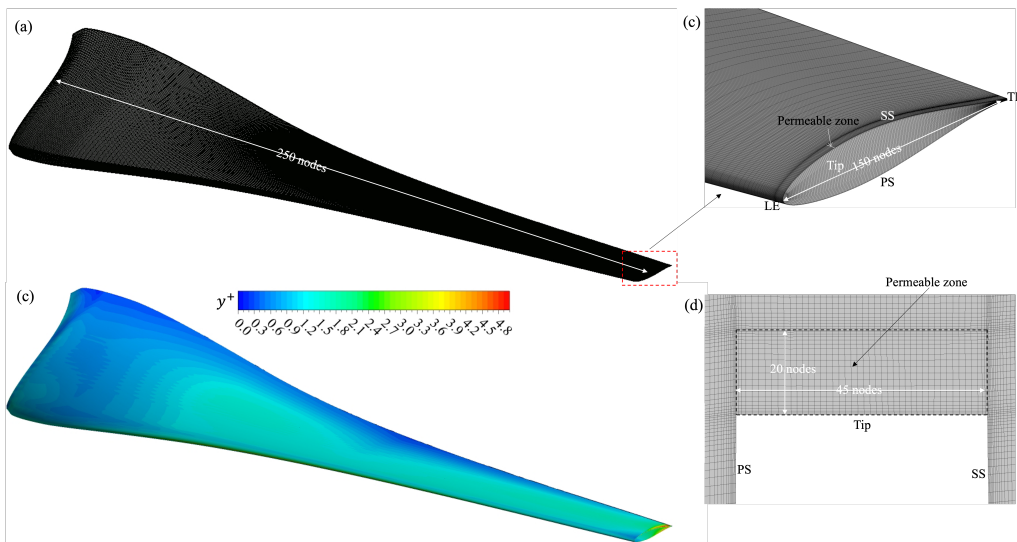


Figure 3: Mesh distribution: (a) mesh on the blade surface; (b) refined mesh near the tip; (c) y^+ distribution on the blade surface; (d) mesh on a cut-section inside the permeable zone. LE: leading edge; TE: trailing edge; PS: pressure side; SS: suction side.

where μ is the dynamic viscosity, κ is the permeability, and \mathbf{u} is the velocity vector.

When this sink term is incorporated into the Navier–Stokes equations and subsequently non-dimensionalised, it results in the form of the following Darcy equation (Neale and Nader (1974); Bose et al. (2023)):

$$\frac{\partial \mathbf{u}}{\partial t} + (\mathbf{u} \cdot \nabla) \mathbf{u} = -\nabla p + \frac{1}{Re} \nabla^2 \mathbf{u} - \frac{1}{Re Da} \mathbf{u} \quad (1)$$

A uniform permeability κ is considered throughout the porous zone, the effect of which is characterized by the non-dimensional parameter Darcy number ($Da = \kappa/\bar{\tau}^2$), where τ is the tip thickness (shown in Figure 1) and its averaged value is $0.26\%D$ along the chordwise direction.

This study is carried out for various Da values in the range of 10^{-4} to 10^{-7} , respectively. The spanwise extent of the porous zone is in the order of $0.1\%D$, and different spanwise extents have been investigated in the present work.

3. Verification and Validation

3.1. Uncertainty assessment

We assess the uncertainty following the least square approach proposed by Viola, Bot and Riotte (2013) and applied in our previous simulation work on a tidal turbine rotor (Liu, Gambuzza, Broglia, Young, McCarthy and Viola (2023)).

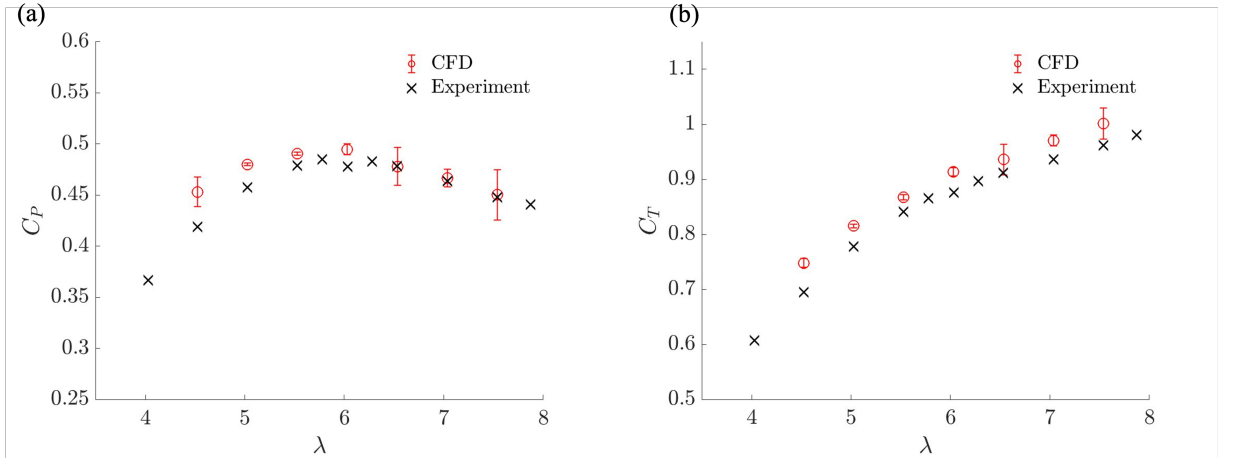


Figure 4: Comparison between CFD and experimental data (Willden et al. (2023)): (a) Power coefficient C_p versus the tip-speed ratio λ ; (b) Thrust coefficient C_T versus the tip-speed ratio λ .

To quantify the reliability of the CFD predictions, we estimate the numerical uncertainty associated with each computed quantity of interest, denoted as Φ , representing either the power coefficient C_p or the thrust coefficient C_T . The uncertainty is expressed in both absolute (E_Φ) and relative (U_Φ) forms at a 95% confidence level, with the relationship defined as

$$E_\Phi = \Phi U_\Phi, \quad (2)$$

The total relative numerical uncertainty U_Φ accounts for several potential error sources, including discretization error due to finite grid resolution (U_{Φ_g}), time stepping (U_{Φ_t}), round-off error (U_{Φ_r}), and convergence error from the iterative solver (U_{Φ_c}). In this work, since the simulations are steady-state and use double precision, $U_{\Phi_r} = 0$ and U_{Φ_c} is considered negligible.

To evaluate the spatial discretisation uncertainty, simulations are performed using four sets of grid resolutions, spanning from 5.64×10^6 cells to 3.01×10^7 cells. A normalised metric is introduced as

$$\varphi(h) \equiv \frac{\Phi(h)}{\Phi(\text{base})}, \quad (3)$$

where h represents the relative grid size and $\Phi(\text{base})$ is the solution obtained with the base mesh. The relationship $\varphi(h)$ is approximated by a power-law fit of the form

$$\varphi(h) \approx \zeta h^\xi + \varphi_0, \quad (4)$$

where the coefficients are either directly computed using the available data points or estimated via least-squares regression. The standard deviation σ of the fit quantifies the fitting error.

Depending on the fit quality p , the relative uncertainty due to grid resolution is calculated as:

$$U_{\Phi_g} = \begin{cases} 1.25 |1 - \varphi_0| + \sigma, & \text{if } p \geq 0.95, \\ 1.5 \frac{\varphi_{\max} - \varphi_{\min}}{1 - \frac{h_{\min}}{h_{\max}}} + \sigma, & \text{if } p < 0.95, \end{cases} \quad (5)$$

where φ_{\max} and φ_{\min} are the extrema of $\varphi(h)$, and h_{\max} , h_{\min} are the corresponding step sizes.

The convergence error is estimated by fitting the solution history over 4000 iterations (excluding the first 2000) with an asymptotic function. The error is defined as the difference between the final solution and the asymptotic limit, scaled by a safety factor of 1.25, and augmented by the standard deviation of the fit.

The total relative numerical uncertainty is computed as:

$$U_{\Phi} = \sqrt{U_{\Phi_g}^2 + U_{\Phi_t}^2 + U_{\Phi_r}^2} + U_{\Phi_c}, \quad (6)$$

noting that U_{Φ_c} is not included under the square root because it is not considered to be independent of the other terms.

Simulations were carried out for a range of tip-speed ratios from 4.52 to 7.54. Figure 4 shows C_P and C_T computed with CFD and the experimental data (Willden et al. (2023)) and the numerical uncertainty of CFD. The relative error in the CFD predictions of C_P is 1.1% at the design tip speed ratio $\lambda = 6.03$, while it is higher both at low and high tip speed ratios, shown in Figure 4a. At low tip-speed ratios, the error is up to 3.2% at $\lambda = 4.52$, and it might be attributed to underpredicted flow separation. The overall numerical uncertainty is between 0.28% to 5.4% for C_P , including the grid uncertainty U_{Φ_g} between 0.28% to 5.4% and the convergence uncertainty U_{Φ_c} between 0.01% and 0.52%. As shown in Figure 4b, the relative error of the CFD in predicting C_T is always within 3.0%, taking account into the grid uncertainty U_{Φ_g} between 0.4% to 2.97% and the convergence uncertainty U_{Φ_c} between 0.05% and 0.3% for C_T .

3.2. Water tunnel experiment

In addition, we have performed Particle Image Velocimetry (PIV) experiments in a water tunnel on a half-wing model, which was extruded from the blade-tip profile of the aforementioned turbine. For further details about the experiment setup, please refer to Appendix A.

Numerical simulation on the half-wing model with the same configuration and flow conditions has been performed with the same CFD approach described in Section 2. The distribution of the pithwise velocity v and spanwise velocity w on the cross-section of $x/c = 1.3$ is compared between the CFD and PIV. Figure 5 shows good agreement between the simulation result and experiment result, which demonstrates that the employed CFD approach can accurately predict the mean flow fields within the tip vortices.

3.3. Permeability modelling validation

Since no experimental data currently exist for permeable blade tip configurations, given that this is a novel concept introduced in our work, we have conducted a verification study for a porous (permeable) disk configuration against validated results available in existing studies (Cummins, Viola, Mastropaolo and Nakayama (2017); Roos and Willmarth (1971)). The detailed description of the permeable disk case and simulation setup is described in Appendix B.

The outcomes of this verification study are presented in Figure 6, which demonstrates good agreement between our numerical predictions and those reported in the literature for the predicted drag coefficients. When $Da \rightarrow 0$, the disk becomes effectively impermeable, and the predicted drag coefficient C_D approaches the value corresponding to a solid disk. Conversely, as $Da \rightarrow \infty$, the predicted C_D tends toward zero due to the absence of resistance in the permeable region. This trend is consistently observed in both our simulation results using the Darcy model and in existing literature. This further supports the reliability of our implementation of the porous zone modelling approach in our present work.

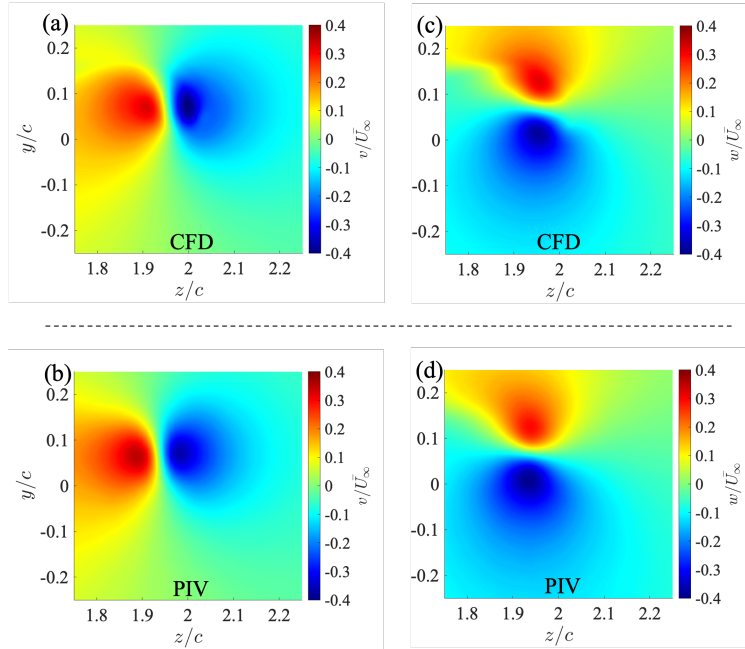


Figure 5: Comparison of the pithwise velocity v ((a), (b)) and spanwise velocity w ((c), (d)) on the cross-section of $x/c = 1.3$ between CFD ((a), (c)) and PIV ((b), (d)). U_∞ denotes the freestream velocity in the water tunnel.

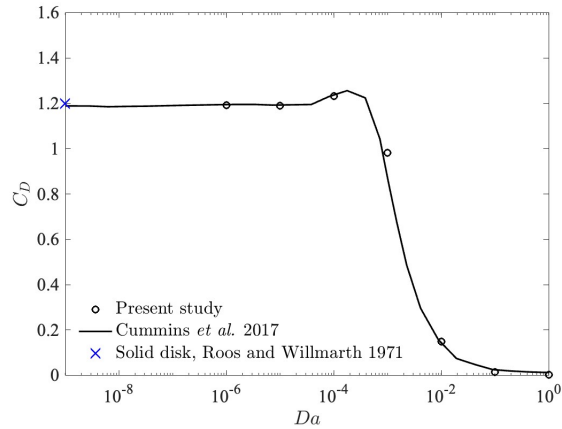


Figure 6: Drag coefficient C_D versus Darcy number Da , in comparison with the results permeable disks from Cummins et al. (2017) and impermeable (solid) disks from Roos and Willmarth (1971).

4. Results and Discussion

4.1. Vortex pattern

Figure 7 shows the comparison of tip vortices, including tip separation vortex (TSV) and PTV, between the baseline case, which is the original turbine without tip permeability, and the permeable tip case, as described in Section 2 and Figure 1 where $Da = 10^{-5}$ and $\zeta = 0.1\%D$. The permeable tip treatment leads to a prominent mitigation of PTV and associated pressure-drop at the vortex core compared to the baseline case. Though the TSV remains visible, the corresponding low-pressure distribution is diminished, caused by the reduced flow separation at the pressure-side edge of the blade tip as demonstrated in Figure 8.

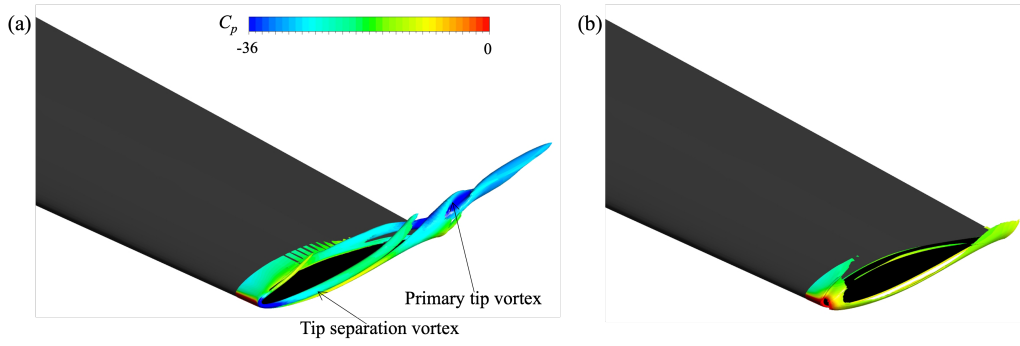


Figure 7: Comparison of 3D vortex pattern between: (a) baseline (without tip permeability); (b) permeable tip with a non-dimensional permeability $Da = 10^{-5}$. The vortex is visualised by the iso-surface of $QD^2/U_\infty^2 = 7.68 \times 10^6$, where Q is the second invariant of the velocity gradient tensor (Q criterion). Pressure-coefficient C_p is defined as $C_p = \frac{p - p_\infty}{\frac{1}{2} \rho U_\infty^2}$, where p_∞ is the inlet pressure and U_∞ is the towing velocity.

Figure 8 demonstrates the surface stream-traces, which are plotted in Tecplot by interpolating the velocity gradients, at the cross-section of 70% chord. The flow fields crossing the permeable zone across a range of Darcy numbers between 10^{-4} and 10^{-6} are presented and discussed. Compared to the baseline case, a significant attenuation of both TSV and PTV is observed for the permeable tip cases, and the local pressure-drop near the vortex cores is suppressed. When the permeability is increased to 10^{-4} , the flow separation near the tip-PS corner again becomes remarkable. When the permeability is decreased to 10^{-6} , a stronger PTV is observed near the suction side. Therefore, there is an optimal range of tip permeability that results in the most effective control of tip vortices.

There are two extreme conditions of tip permeability we can theoretically consider: $Da \rightarrow \infty$ and $Da \rightarrow 0$. For $Da \rightarrow \infty$, the permeable zone presents no resistance to the fluids, and thus it is equivalent to the impermeable blade with a reduced blade span, i.e. the baseline blade with a shorter blade span. Therefore, the vortex pattern (Figure 9a) becomes very close to that in the baseline case, For $Da \rightarrow 0$, the fluids cannot go through the zone at all, so the flow field recovers to the same as that around the baseline blade, shown in Figure 9b.

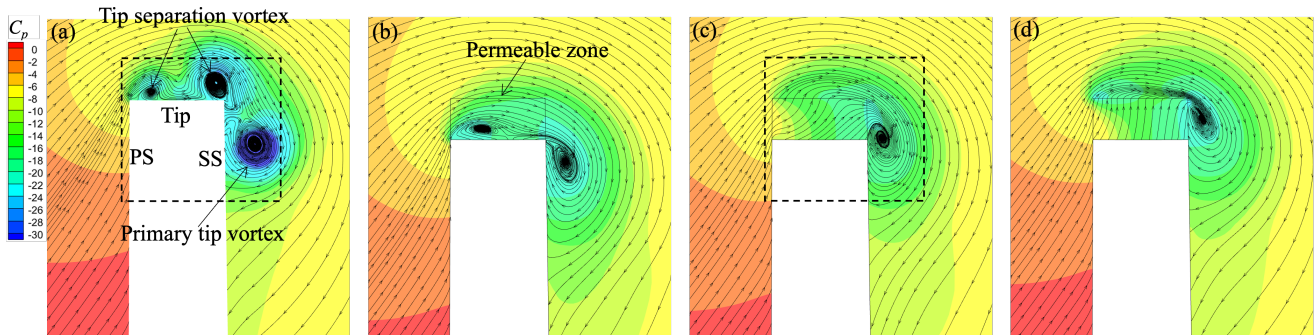


Figure 8: Comparison of surface stream-traces (obtained by interpolating the velocity gradients) at the cross-section of 70% chord between: (a) baseline; (b) permeable tip with a non-dimensional permeability $Da = 10^{-4}$; (c) permeable tip with $Da = 10^{-5}$; (d) permeable tip with $Da = 10^{-6}$.

The surface vectors within the dashed-black box on the same cross-section in Figure 8 for the baseline and the permeable tip with $Da = 10^{-5}$ are shown in Figure 10. Compared to Figure 10a, less flow separation is observed at both the pressure-side and suction side around the tip when the permeable tip treatment is applied. A reduced swirling velocity around the PTV core for the permeable tip (Figure 10b) is also found referring to the vector field around the baseline blade. The above discussion suggests that tip permeability contributes to controlling tip vortices by suppressing the flow separation and vortex intensity near the tip.

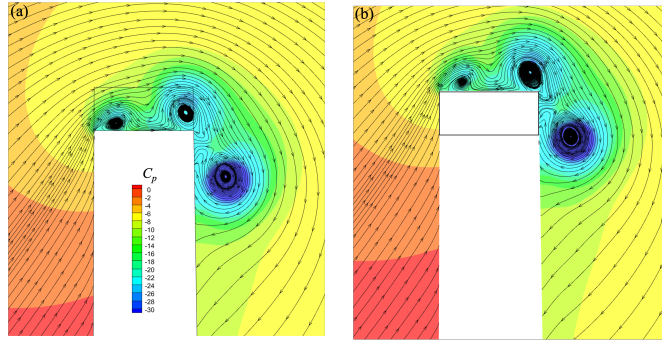


Figure 9: Comparison of surface stream-traces at the cross-section of 70% chord between: (a) $Da \rightarrow \infty$ (b) $Da \rightarrow 0$ (baseline).

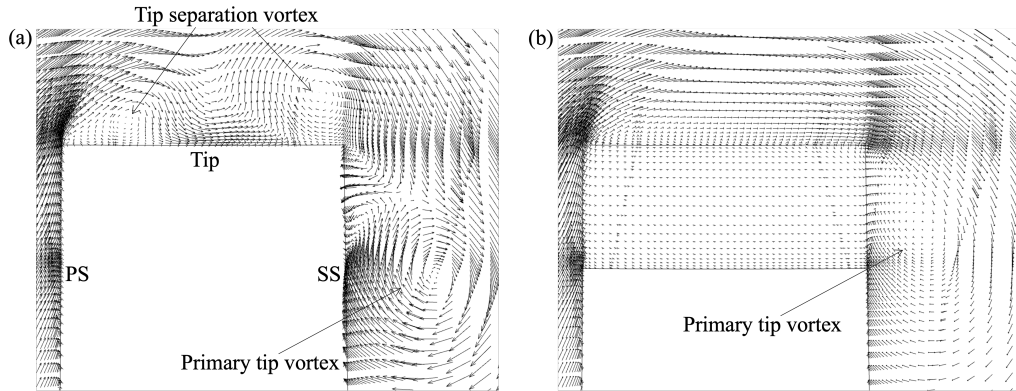


Figure 10: Comparison of surface vectors at the cross-section of 70% chord between: (a) baseline; (b) permeable tip with $Da = 10^{-5}$.

4.2. Pressure-coefficient at the vortex cores

As cavitation is our primary concern in the present work and the most significant pressure-drop occurs at the PTV cores, we focus on the pressure-coefficient C_p along the PTV core trajectory. As illustrated in Figure 11a, we extract the minimal C_p on each cross-section between the mid-chord position of $y/c = 0.5$, where PTV just detached from the blade tip, to $y/c = 1.4$ in the wake region.

We further plot the distribution of the extracted minimal pressure-coefficient $C_{p_{\min}}$ along the PTV core trajectory (Figure 11b). It is demonstrated that there is an optimal range of permeability, corresponding to Da around 10^{-5} , that can substantially reduce the tip vortex intensity and associated pressure-drop. This finding aligns well with the discussion on the vortex pattern with different tip permeability in Section 4.1. The lowest value of $C_{p_{\min}}$ along the PTV core trajectory is found to be -45.7, and the permeable tip with $Da = 10^{-5}$ increases it to -22.0, which means a relative change of 52%.

A further investigation into the effects of tip permeability across different TSRs and different spanwise extent of the permeable zone is presented in Figure 12. Between $\lambda = 4.52$ to $\lambda = 7.54$, all the results show a remarkable mitigation of the pressure-drop at the PTV cores, and the permeable tip treatment with $Da = 10^{-5}$ always show the optimal effect. Even promisingly, the mitigation effect becomes more significant at higher TSRs, and the relative increase of $C_{p_{\min}}$ reaches 63%.

These results demonstrate the great promise of using tip permeability to mitigate tip vortices and their cavitation risks, which will significantly contribute to breaking the current TSR limit capped by blade-tip cavitation.

In addition, the influence of the permeable zone's spanwise extent is also considered and discussed in Appendix C. The results suggest a more prominent mitigation of the pressure-drop with a larger spanwise extent of $\zeta = 0.2\%D$. However, it also leads to a further drop in the power-coefficient while little change is observed for the thrust-coefficient.

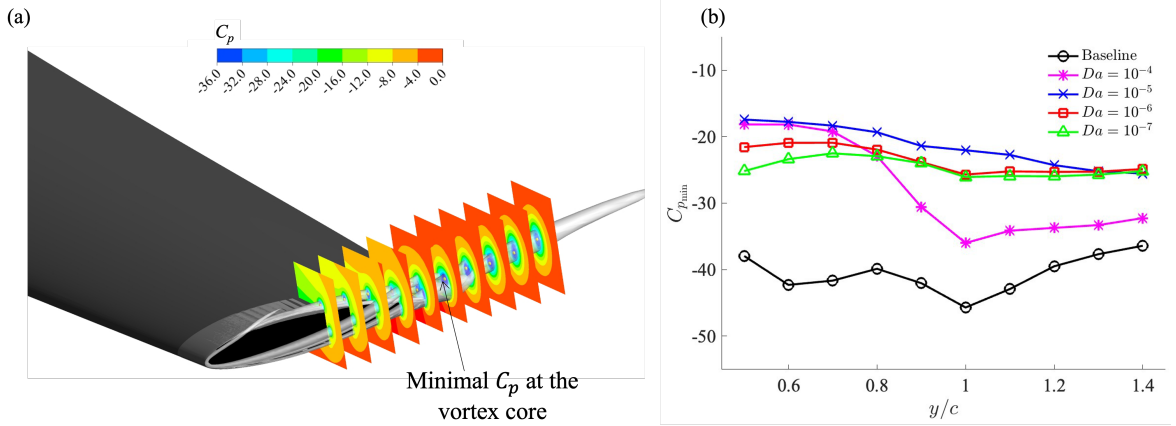


Figure 11: Effect of tip permeability on mitigating pressure-drop: (a) tip vortices visualised by Q criterion and distribution of pressure-coefficient C_p on cross-sections across a range of chord ratios (b) comparison of minimal pressure-coefficient $C_{p_{\min}}$ along the PTV core trajectory between the baseline blade and the blade with different tip permeability. The tip speed ratio is 6.03.

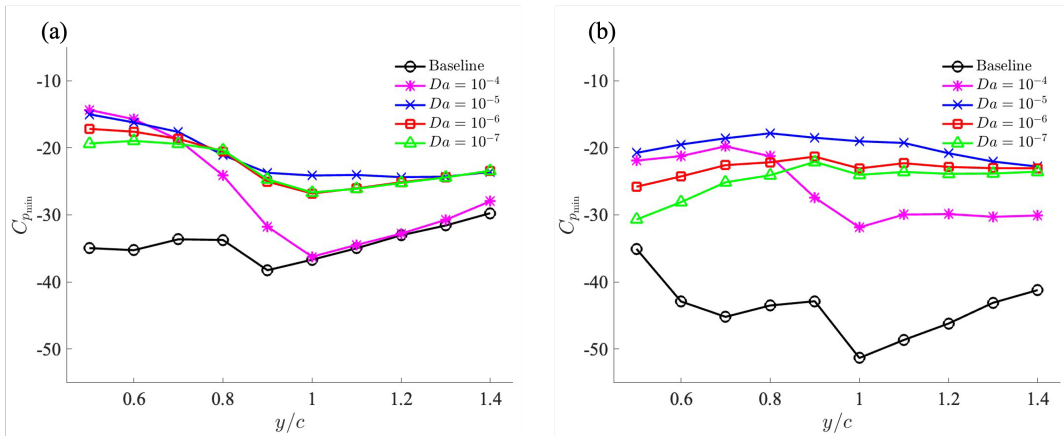


Figure 12: Comparison of minimal pressure-coefficient $C_{p_{\min}}$ along the PTV core between the baseline and the permeable tip at the tip speed ratio of: (a) $\lambda = 4.52$ (b) $\lambda = 7.54$.

Therefore, there is a trade-off between mitigating tip vortices and ensuring a positive or negligible influence on the turbine's power and thrust performance.

4.3. Power and thrust performance

In this section, we discuss the influence of permeable tip treatment on the turbine's power and thrust performance. Simulations with and without the permeable tip show that the power-coefficient C_p of the turbine with a permeable tip ($Da = 10^{-5}$; $\zeta = 0.1\%D$) drops by 0.25% at $\lambda = 4.52$, 0.75% at $\lambda = 6.03$, and 0.17% at $\lambda = 7.53$ compared to the baseline turbine (Figure 13a). This suggests a negative but negligible influence on the turbine power-coefficient under non-cavitation conditions.

However, the thrust-coefficient C_T decreases by 0.68% at $\lambda = 4.52$, 1.06% at $\lambda = 6.03$, and 0.72% at $\lambda = 7.53$ compared to the baseline turbine (Figure 13b). A decreased C_T is beneficial to reduce the levelised cost of energy for turbines, because it can allow reduced the structural loads, simplified powertrains and increased turbine lifespan. Moreover, the drop of C_T is more significant than that of C_p . Therefore, the overall influence of tip permeability on the turbine's power-thrust performance is positive but limited.

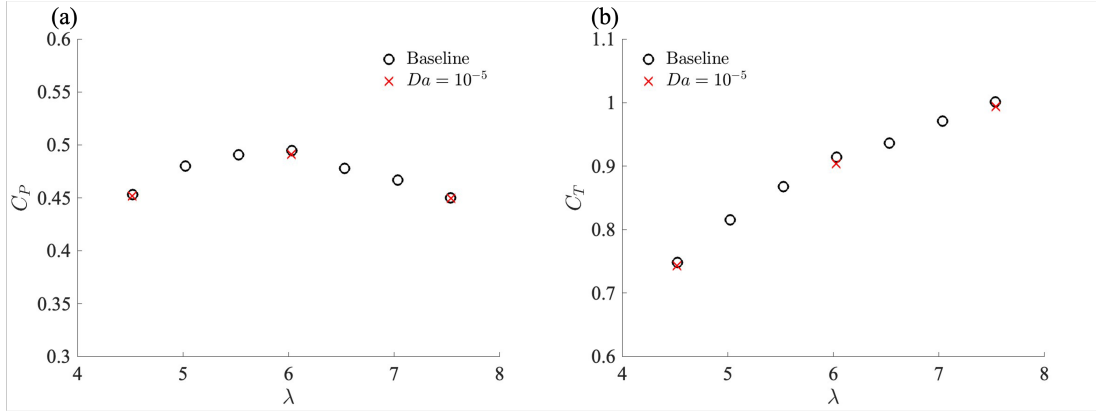


Figure 13: Comparison of (a) power-coefficient C_p and (b) thrust-coefficient C_T between baseline and permeable tip with $Da = 10^{-5}$ across a range of tip speed ratio λ between 4.52 and 7.54.

4.4. Vortex parameters and flow physics

To understand the underlying physics of how tip permeability reduces the intensity of tip vortices and associated pressure-drop, the vortex parameters are investigated in this section. Following the method applied by Matthieu (2015), we analyse the minimum pressure-coefficient $C_{p_{\min}}$ and the non-dimensional vortex intensity $\Gamma/(r_c U_{\text{tip}})$ at each cross-section, according to the following equation:

$$C_{p_{\min}} = -\beta \left(\frac{\Gamma}{r_c U_{\text{tip}}} \right)^2 \quad (7)$$

where Γ is the circulation of the vortex; $U_{\text{tip}} = U_{\infty} \sqrt{1 + \lambda^2}$ is the flow speed near the blade tip; r_c is the viscous core radius where the maximal swirling velocity is reached; β is a constant whose value depends on the choice of vortex model, and a Rankine vortex model is considered in the present work and $\beta = (2\pi^2)^{-1}$. In the present work, Γ on each cross-section is computed by integrating the vorticity ω over an area where ω exceeds a specific threshold. As the boundary vorticity increases, the integrated circulation asymptotically approaches a limit. The threshold is selected when 99% of the circulation is included.

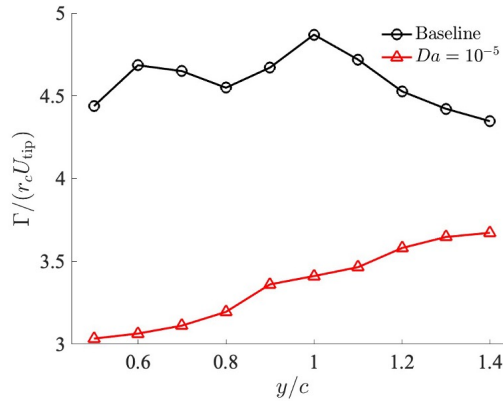


Figure 14: Comparison of non-dimensional vortex intensity $\Gamma/(r_c U_{\text{tip}})$ on each cross-section along the vortex core trajectory between baseline and permeable tip with $Da = 10^{-5}$. r_c denotes vortex viscous core radius and Γ denotes circulation. The tip speed ratio is 6.03.

Controlling Vortices through Tip Permeability

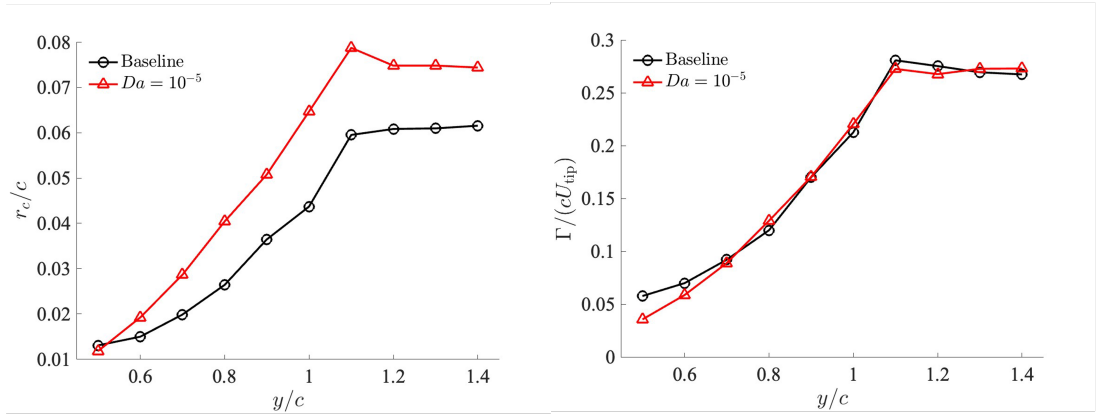


Figure 15: Comparison of: (a) vortex viscous core radius r_c (normalised by the blade-tip chord length c) (b) vortex circulation Γ on each cross-section (normalised by c and the flow speed U_{tip} near the blade tip) along the vortex core trajectory between baseline and permeable tip with $Da = 10^{-5}$. The tip speed ratio is 6.03.

The non-dimensional vortex intensity $\Gamma/(r_c U_{tip})$ on each cross-section is extracted from the simulation and plotted along the PTV core trajectory in Figure 14. The permeable tip case shows a significant drop in the non-dimensional vortex intensity compared to the baseline case, which corresponds to the reduction of $C_{p_{min}}$ in Figure 11b.

We further investigate the vortex radius r_c and the circulation Γ on each cross-section and plot them along the PTV core trajectory, respectively. On the one hand, as shown in Figure 15a, the vortex radius is enlarged when the permeable tip is applied compared to the baseline case, which is also evident in the 3D streamlines released from the blade tip (Figure 16). On the other hand, there is little change in the circulation of PTV along the vortex core trajectory. These findings inform that the effective mitigation of vortex intensity through permeable tip treatment is mainly contributed by the enlarged radial dimension of the vortex. As illustrated in the comparison of 3D streamlines between the baseline (Figure 16a) and the permeable tip (Figure 16b), the application of a permeable tip results in a significant diffusion of the vortex over a larger area, thereby reducing its intensity. Consequently, the pressure-drop at the vortex core is mitigated.

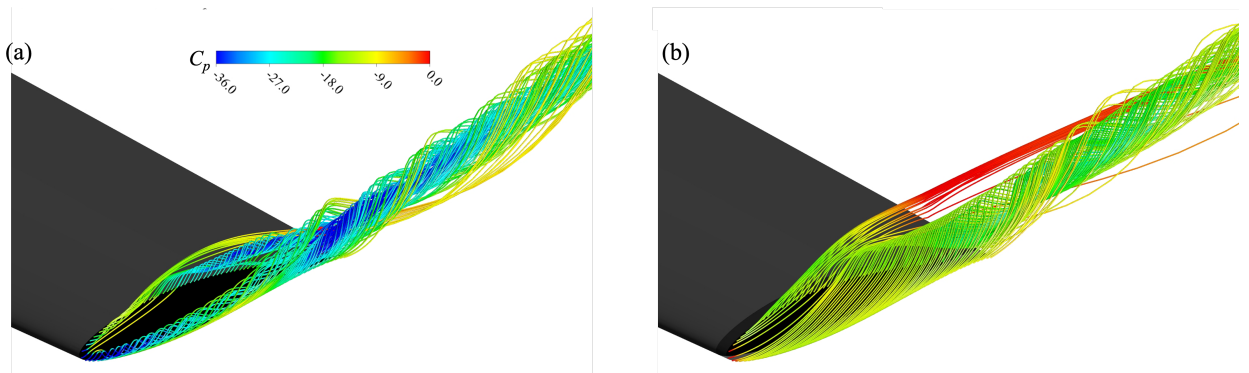


Figure 16: Comparison of 3D streamlines released from the blade tip between: (a) baseline; (b) permeable tip with $Da = 10^{-5}$ at a tip speed ratio of 6.03.

5. Conclusion and Future Work

This work presents a novel passive, small-scale flow control strategy that introduces local permeability at the blade tip to mitigate trailing tip vortices and associated pressure drops, which can lead to cavitation. Unlike traditional methods that modify blade geometry or employ active control techniques, this study demonstrates that introducing a

thin permeable zone—occupying only 0.1% of the turbine diameter—can substantially alter the vortex dynamics while preserving the performance of blade-based systems.

A broad parametric analysis across tip-speed ratios ($TSR = 4.52\text{--}7.54$) for a model-scale tidal turbine and Darcy numbers ($Da = 10^{-4}\text{--}10^{-7}$) reveals that optimal mitigation occurs at approximately $Da = 10^{-5}$. At this level of permeability, the tip vortex intensity is significantly reduced due to an enlarged vortex viscous core radius, while the circulation remains nearly unchanged. This leads to enhanced vortex diffusion, which in turn reduces the minimum suction pressure coefficient in the vortex core by up to 63%, greatly mitigating cavitation risk.

The novelty of this work lies in identifying a new physical mechanism for vortex control—namely, the manipulation of tip vortex structure through local permeability without compromising the hydrodynamic performance of the blades. Furthermore, the consistent performance of the mitigation effect across a wide range of TSRs indicates its robustness and applicability to real-world operating conditions. The minimal impact on power and thrust coefficients (less than 1% in all cases) underscores the practical feasibility of this approach.

These findings provide a new direction for passive flow control via material and structural design. The concept of controlling tip vortices through permeability has broader implications for improving the aerodynamic and hydrodynamic performance of turbines, propellers, drones, and lifting surfaces in both underwater and aerial environments.

A critical next step in this research is to deepen our understanding of the unsteady fluid dynamics, particularly the complex interactions among tip vortices, cavitation clouds, and the permeable tip structure. In particular, coupling high-fidelity approaches, such as Large Eddy Simulation (LES) with cavitation models, will be essential. The advanced cavitation modelling frameworks developed by Zhao, Cheng, Ji, Li and Bensow and Wang, Bai, Cheng, Ji and Peng offer promising tools to capture these intricate dynamics with improved accuracy.

Furthermore, future work will explore experimental validation and structural implementation strategies to replicate the permeable effect, starting from simplified foil models and progressing towards turbine blades. In addition, we aim to extend this concept to the control of wake dynamics and noise generation, with potential applications across a range of turbomachinery systems and the design of aerial and underwater vehicles.

However, while the concept of flow control with permeable structures is fundamentally novel and shows strong potential, its practical implementation may require high-precision manufacturing to realise fine-scale permeable structures. Furthermore, potential issues such as biofouling, local blockage, and long-term structural durability in harsh marine environments are important considerations. These challenges highlight the need for interdisciplinary collaboration across fluid dynamics, advanced manufacturing, structural mechanics, and materials science to advance this concept toward real-world application.

CRedit authorship contribution statement

Yabin Liu: Conceived, designed, and supervised the project; led the development of the numerical model and the data analysis; wrote the first draft of the manuscript.. **Junchen Tan:** Prepared and performed the experiments, post-processed the experimental data, and edited the manuscript.. **Richard H. J. Willden:** Co-supervised the project, advised on the analysis of the results, and edited the manuscript.. **Paul Gary Tucker:** Co-supervised the project, advised on the simulations, and edited the manuscript.. **Ignazio Maria Viola:** Co-supervised the project, advised on the experiments and simulations, and edited the manuscript..

Acknowledgments

This work has been supported by the Royal Commission for the Exhibition of 1851 Brunel Fellowship (Yabin Liu), the UK EPSRC-funded Supergen Offshore Renewable Energy Hub [EP/Y016297/1], the Royal Society ISPF-International Collaboration Award [ICA/R1/231053], EPSRC Standard Proposal [EP/V009443/1], and the EPSRC IAA Innovation Competition [EPSRC IAA PV111].

Author Declarations

Conflict of Interest

The authors have no conflicts to disclose.

Data Availability

Data will be made available on request.

References

- Arcondoulis, E., Liu, Y., Ragni, D., Avallone, F., Rubio-Carpio, A., Sedaghatizadeh, N., Yang, Y., Li, Z., 2023. Internal shear layer and vortex shedding development of a structured porous coated cylinder using tomographic particle image velocimetry. *Journal of Fluid Mechanics* 967, A17.
- Bai, X., Cheng, H., Ji, B., 2022. Les investigation of the noise characteristics of sheet and tip leakage vortex cavitating flow. *International Journal of Multiphase Flow* 146, 103880.
- Bi, Z., Bao, F., Zhang, L., Shao, X., Li, S., 2024. Numerical study of porous tip treatment in suppressing tip clearance vortices in cavitating flow. *Physics of Fluids* 36.
- Bose, C., Bruce, C., Viola, I.M., 2023. Porous plates at incidence. arXiv preprint arXiv:2303.13296 .
- Coles, D., Angeloudis, A., Greaves, et al., 2021. A review of the uk and british channel islands practical tidal stream energy resource. *Proceedings of the Royal Society A* 477, 20210469.
- Cummins, C., Seale, M., Macente, A., Certini, D., Mastropaolo, E., Viola, I.M., Nakayama, N., 2018. A separated vortex ring underlies the flight of the dandelion. *Nature* 562, 414–418.
- Cummins, C., Viola, I.M., Mastropaolo, E., Nakayama, N., 2017. The effect of permeability on the flow past permeable disks at low reynolds numbers. *Physics of Fluids* 29.
- Dreyer, M., Decaix, J., Münch-Alligné, C., Farhat, M., 2014. Mind the gap: a new insight into the tip leakage vortex using stereo-piv. *Experiments in fluids* 55, 1–13.
- Fiscaletti, D., Pereira, L.T.L., Ragni, D., 2024. Finlet rails for the reduction of the trailing-edge noise. *Journal of Sound and Vibration* 568, 118072.
- Global Wind Energy Council, 2024. Global Wind Report 2024. URL: <https://gwec.net/global-wind-report-2024/>. accessed: 2024-06-19.
- Han, Y., Liu, Y., Tan, L., 2022. Method of variable-depth groove on vortex and cavitation suppression for a naca0009 hydrofoil with tip clearance in tidal energy. *Renewable Energy* 199, 546–559.
- Hou, G., Ren, Y., Zhang, X., Dong, F., An, Y., Zhao, X., Zhou, H., Chen, J., 2020. Cavitation erosion mechanisms in co-based coatings exposed to seawater. *Ultrasonics Sonochemistry* 60, 104799.
- Jiang, J.W., Xie, C.M., Xu, L.H., Li, L., Huang, W.X., 2022. The groove at blade tip designed for suppression of tip-leakage vortex may bring the risk of inducing new cavitation. *Physics of Fluids* 34.
- Khorrani, M.R., Li, F., Choudhari, M., 2002. Novel approach for reducing rotor tip-clearance-induced noise in turbofan engines. *AIAA journal* 40, 1518–1528.
- Lignarolo, L., Ragni, D., Scarano, F., Ferreira, C.S., Van Bussel, G., 2015. Tip-vortex instability and turbulent mixing in wind-turbine wakes. *Journal of Fluid Mechanics* 781, 467–493.
- Liu, Y., Gambuzza, S., Broglia, R., Young, A., McCarthy, E., Viola, I.M., 2023. On the accuracy of bemt and cfd on the power and trust prediction of tidal turbines, in: *The 15th European Wave and Tidal Energy Conference*.
- Liu, Y., Tan, L., 2018. Method of c groove on vortex suppression and energy performance improvement for a naca0009 hydrofoil with tip clearance in tidal energy. *Energy* 155, 448–461.

- Liu, Y., Tan, L., 2020. Influence of c groove on suppressing vortex and cavitation for a naca0009 hydrofoil with tip clearance in tidal energy. *Renewable Energy* 148, 907–922.
- Liu, Y., Tan, L., Wang, B., 2018. A review of tip clearance in propeller, pump and turbine. *Energies* 11, 2202.
- Liu, Y., Wang, Z.N., Tan, L., Tucker, P.G., Möller, F.M., 2024. Tip-leakage-flow excited unsteadiness and associated control. *Physics of Fluids* 36.
- Matthieu, D., 2015. Mind the gap: Tip leakage vortex dynamics and cavitation in axial turbines. Ph.D. thesis. Lausanne, Switzerland: École Polytechnique Fédérale de Lausanne.
- Muir, R.E., Arredondo-Galeana, A., Viola, I.M., 2017. The leading-edge vortex of swift wing-shaped delta wings. *Royal Society Open Science* 4, 1–14.
- Neale, G., Nader, W., 1974. Practical significance of Brinkman's extension of Darcy's law: coupled parallel flows within a channel and a bounding porous medium. *The Canadian Journal of Chemical Engineering* 52, 475–478.
- Ning, A., Dykes, K., 2014. Understanding the benefits and limitations of increasing maximum rotor tip speed for utility-scale wind turbines, in: *Journal of physics: conference series*. IOP Publishing. p. 012087.
- Palleja-Cabre, S., Saraceno, I., Paruchuri, C.C., Joseph, P., 2022. Reduction of tip-leakage noise by using porosity, in: *28th AIAA/CEAS Aeroacoustics 2022 Conference*, p. 3061.
- Posa, A., Broglia, R., Balaras, E., 2021. Instability of the tip vortices shed by an axial-flow turbine in uniform flow. *Journal of Fluid Mechanics* 920, A19.
- Posa, A., Viola, I.M., Broglia, R., 2024. Influence of the tip speed ratio on the wake dynamics and recovery of axial-flow turbines. *Physics of Fluids* 36.
- Ramachandran, R.C., Raman, G., Dougherty, R.P., 2014. Wind turbine noise measurement using a compact microphone array with advanced deconvolution algorithms. *Journal of Sound and Vibration* 333, 3058–3080.
- Roos, F.W., Willmarth, W.W., 1971. Some experimental results on sphere and disk drag. *AIAA journal* 9, 285–291.
- Viola, I.M., Bot, P., Riotte, M., 2013. On the uncertainty of cfd in sail aerodynamics. *International journal for numerical methods in fluids* 72, 1146–1164.
- Wang, X., Bai, X., Cheng, H., Ji, B., Peng, X., 2023. Numerical investigation of how gap size influences tip leakage vortex cavitation inception using a eulerian–lagrangian method. *Physics of Fluids* 35.
- Wang, X., Bai, X., Qian, Z., Cheng, H., Ji, B., 2022. Modal analysis of tip vortex cavitation with an insight on how vortex roll-up enhances its instability. *International Journal of Multiphase Flow* 157, 104254.
- Willden, R., Chen, X., Harvey, S., Edwards, H., Vogel, C., Bhavsar, K., Allsop, T., Gilbert, J., Mullings, H., Ghobrial, M., et al., 2023. Tidal turbine benchmarking project: Stage I-Steady flow blind predictions. Technical Report. National Renewable Energy Laboratory (NREL), Golden, CO (United States).
- Wimshurst, A., Vogel, C., Willden, R., 2018. Cavitation limits on tidal turbine performance. *Ocean Engineering* 152, 223–233.
- Ye, Q., Wang, Y., Shao, X., 2023. Dynamics of cavitating tip vortex. *Journal of Fluid Mechanics* 967, A30.
- Zhao, X., Cheng, H., Ji, B., Li, L., Bensow, R.E., 2024. Insights into the characteristics of sheet/cloud cavitation and tip-leakage cavitation based on a compressible euler-lagrange model. *Physical Review Fluids* 9, 104304.

A. Water tunnel experiments on a half-wing model

To validate the accuracy of the employed CFD approach on predicting tip vortices, PIV experiments were conducted in a water tunnel on a half-wing model, extruded from the blade-tip profile of the same turbine (Willden et al. (2023)). The water tunnel located at the University of Edinburgh is 8 m long, 0.4 m wide, and filled with water to 0.4 m depth, as shown in Figure 17. The flow is preconditioned by curving vanes before entering and exiting the channel. The half-wing model has a chord length of $c = 0.1$ m and a span of $b = 0.2$ m. The coordinate system $x - y - z$ shows the streamwise, cross-stream, and spanwise coordinate. The flow velocity was calibrated using a Vectrino acoustic Doppler anemometer at the centre of the measurement plane without the presence of model and underwater cameras. The experiments were performed at a nominal free-stream velocity of $U_\infty = 0.28$ m s⁻¹ (equivalent to a Reynolds number based on the chord length of $Re_c = 3 \times 10^4$) with a streamwise turbulence intensity of approximately 4.5% before the leading edge. The wing's angle of attack is set as 6°

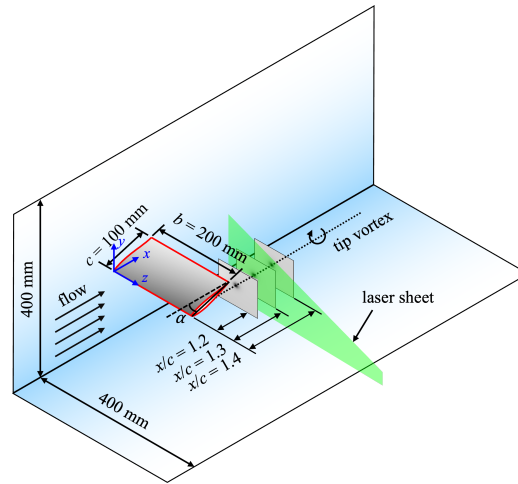


Figure 17: Dimensions of the water tunnel and coordinate system used in the experiments. Displayed contours are obtained from CFD simulation and for illustrative purpose only.

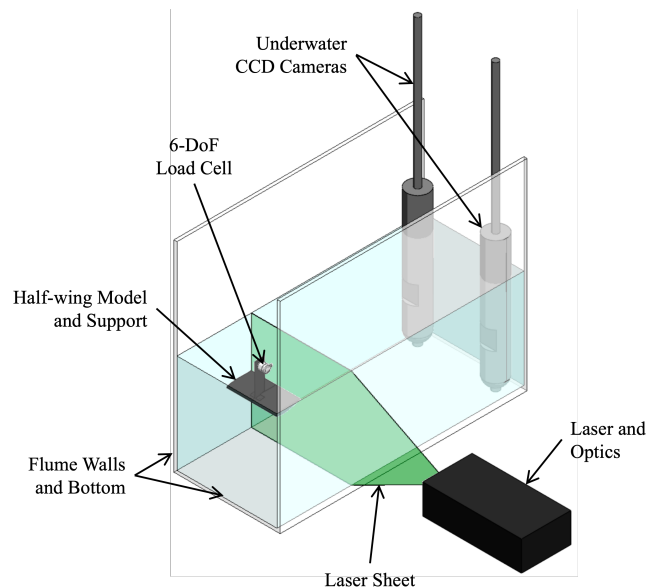


Figure 18: Schematic of experimental setup for particle image velocimetry measurements for cross-flow planes.

The experimental setup for the PIV measurements and the tested sections are schematically shown in Figure 18. For more details, please refer to the work performed by Muir, Arredondo-Galeana and Viola (2017) with the same PIV and underwater camera system. Quantitative flow field analysis was performed using a LaVision FlowMaster Underwater stereoscopic PIV system, and the flow field cross-flow (normal to free-stream) sections at different streamwise locations were measured. For each measurement, 500 snapshots of the instantaneous flow field at each cross-section were utilised at a rate of 7 Hz to accurately account for the mean flow statistics. The interrogation window size was 32×32 pixels with 75% overlap, producing an effective grid size of approximately 1% of the chord length. The uncertainty of the velocity measurements was calculated to be within 2% of the free-stream velocity.

B. Permeable disk simulation

To verify the permeability modelling approach, a validation study is conducted using a three-dimensional permeable disk, with reference to both numerical and experimental data from existing literature. As shown in Figure 19, the disk has a thickness-to-diameter ratio of 10 and is positioned within a cylindrical computational domain that extends 60 disk diameters downstream and 40 disk diameters in the radial direction. The permeable disk is meshed with 100 cells radially, 400 circumferentially, and 20 across its thickness. The Reynolds number, defined using the freestream velocity and disk diameter, is set to $Re = 130$ based on available data from the literature (Cummins et al. (2017); Roos and Willmarth (1971)). Accordingly, a laminar flow model is applied in the permeable disk simulation.

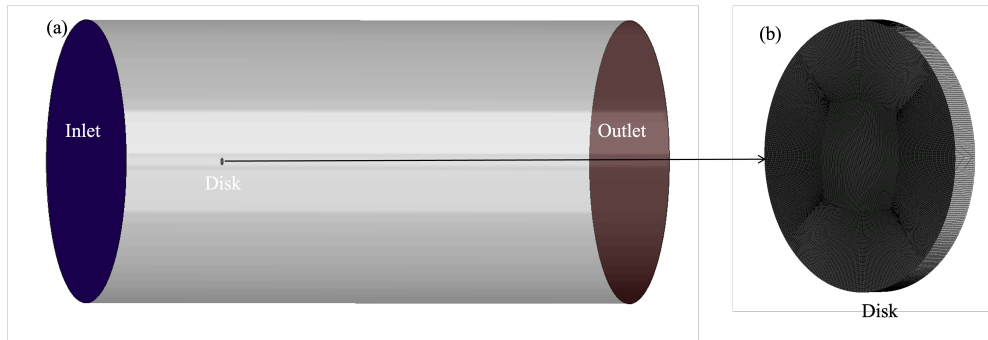


Figure 19: Permeable disk case configuration: (a) computational domain; (b) mesh on the disk.

The same porous media model, based on the Darcy equation and described in Section 2, is employed in this simulation. Drag coefficients of the permeable disk across a range of Darcy numbers have been extracted and compared with validated results from Cummins et al. (2017); Roos and Willmarth (1971).

C. Influence of the spanwise extent of the permeable zone

The effects of the permeable tip with different spanwise extent of the permeable zone are investigated and discussed in this section. Though a more prominent mitigation of the pressure-drop with a larger spanwise extent of $\zeta = 0.2\% D$ (Figure 20a), there is a further drop in the power-coefficient (Figure 20b), while little change is observed for thrust-coefficient (Figure 20c). Therefore, the negative influence on the power performance of the turbine is increased with a larger permeable zone. A trade-off between the effect of mitigating tip vortices and the turbine power-thrust performance should be considered in practical designs.

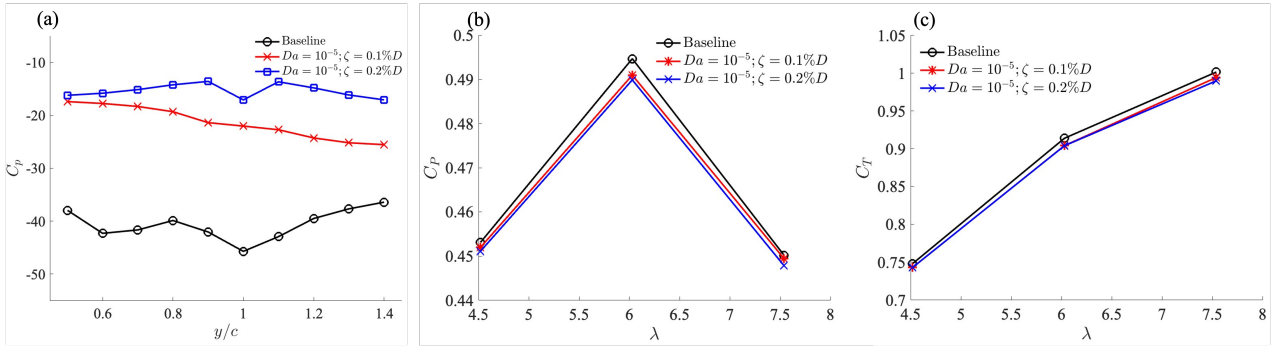


Figure 20: Comparison of: (a) pressure-coefficient C_p along the PTV core (b) power-coefficient C_p (c) thrust-coefficient C_T between $\zeta = 0.1\%D$ and $\zeta = 0.2\%D$. The tip permeability is set as $Da = 10^{-5}$.